Electronic Supplementary Material (ESI) for Green Chemistry.

Electronic Supplementary Information

Lignin-Fueled Photoelectrochemical Platform for Light-Driven Redox Biotransformation

Ding Wang,‡[a] Sahng Ha Lee, ‡[a] Seunghyun Han,[b] Jinhyun Kim,[a] Nguyen Vu Thien Trang,[b]
Kayoung Kim,[a] Eun-Gyu Choi,[b] Passarut Boonmongkolras,[a] Yang Woo Lee,[a] Byungha Shin,[a]
Yong Hwan Kim,*[b] and Chan Beum Park*[a]

[a]Department of Materials Science and Engineering, Korea Advanced Institute of Science and Technology (KAIST), 335 Science Road, Daejeon 305-701, Republic of Korea.
[b]School of Energy and Chemical Engineering, Ulsan National Institute of Science and Technology (UNIST) 50 UNIST-gil, Ulsan 44919, Republic of Korea.
*Corresponding email: metalkim@unist.ac.kr (Y.H.K.), parkcb@kaist.ac.kr (C. B. P.)

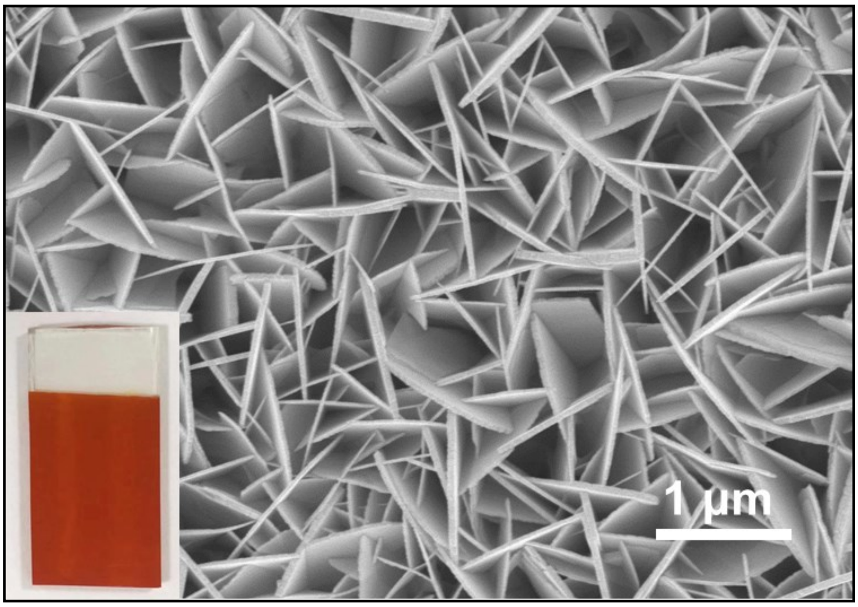

Figure S1. Plan-view scanning electron microscopy (SEM) and photograph image of as-deposited BiOI electrode. The as-synthesized BiOI film exhibited a 2D crystal structure with the morphology of extremely thin plate.

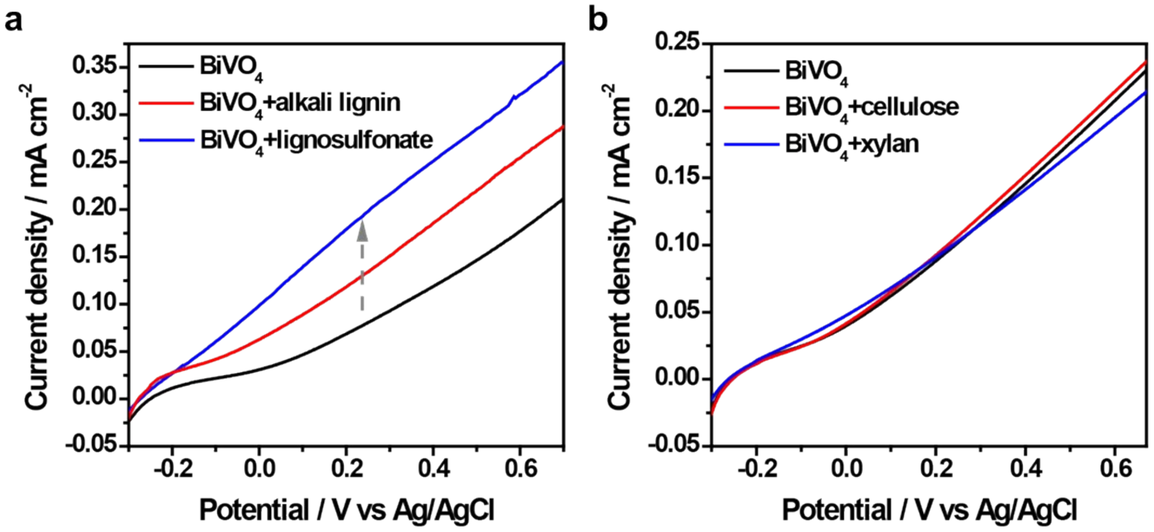

Figure S2. Electrochemical analysis of the $BiVO_4$ photoelectrode. (a) Linear-sweep voltammetric (LSV) of the BiVO4 photoelectrode with alkali lignin and lignosulfonate (1 mg mL^{-1}) under light irradiation (100 mW cm^{-2}). (b) LSVs of $BiVO_4$ with cellulose and xylan (1mg mL^{-1}). Scan rate was 50 mV s^{-1}. Both alkali lignin and lignosulfonate induced the increase in the oxidation photocurrent of $BiVO_4$, which indicate that both lignin could work as hole scavengers. On the other hand, cellulose and xylan had no activity for the photocurrent generation by $BiVO_4$.

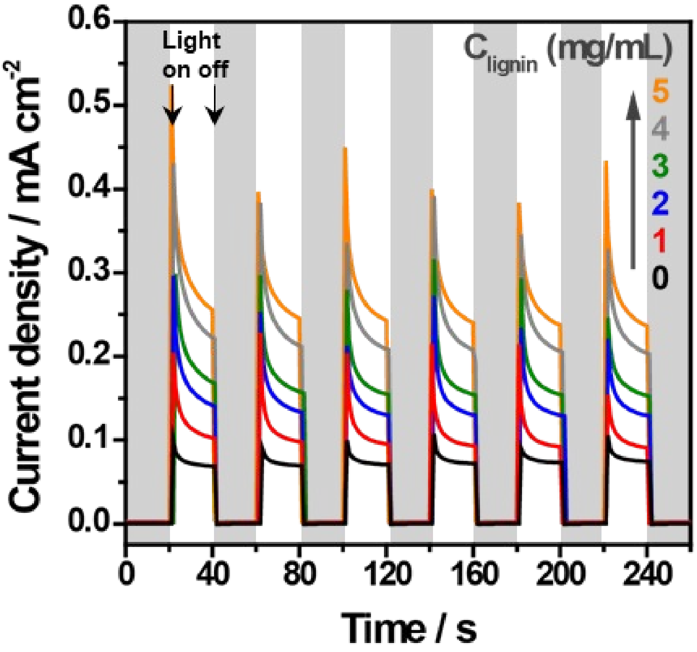

Figure S3. Photocurrent response (J-t curves) of the $BiVO_4$ photoelectrode with various lignin concentrations. Photocurrent was generated under the applied potential of 400 mV (Xe lamp intensity: 100 mW cm^{-2}, scan rate: 50 mV s^{-1}).

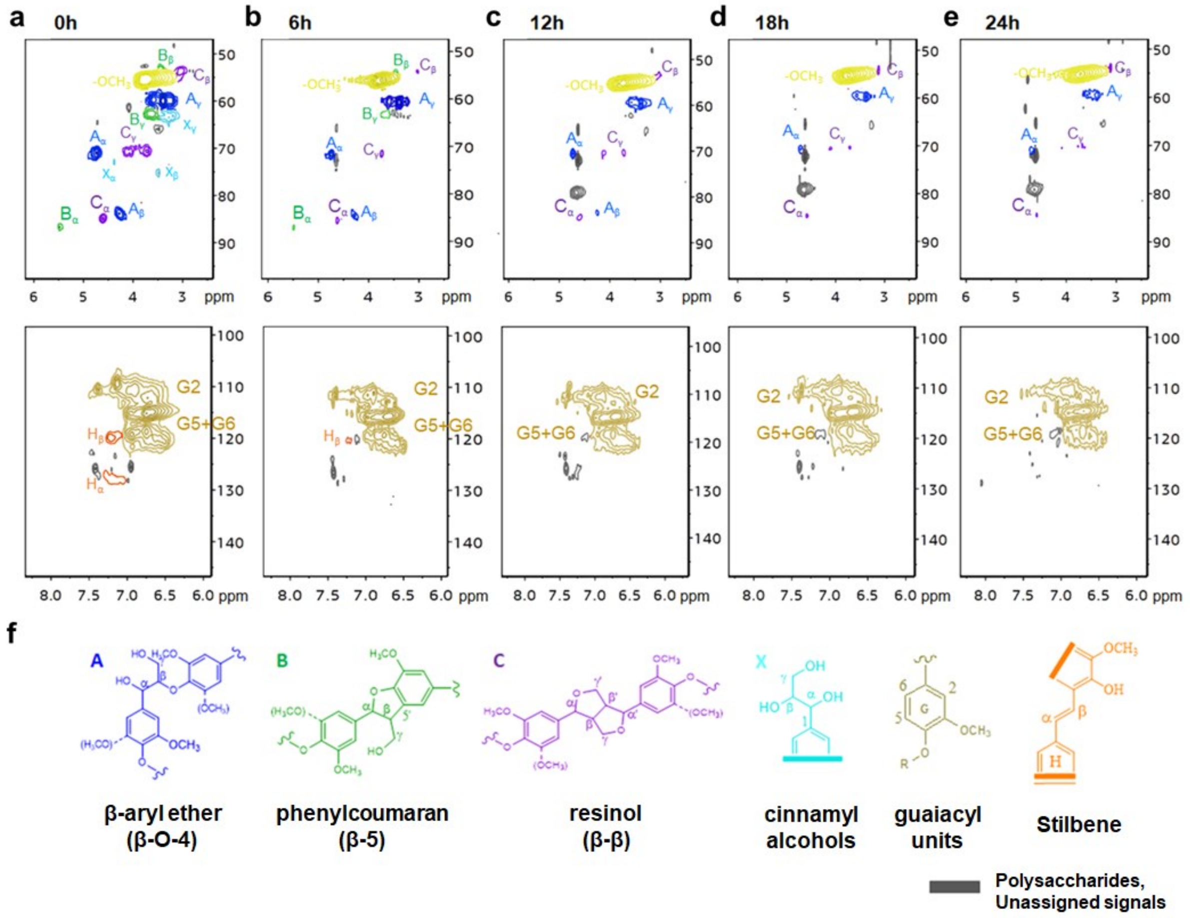

Figure S4. Changes in the chemical structure of alkali lignin during the photoelectrochemical oxidation process monitored by 2-dimentional 13C-1H heteronuclear single-quantum correlation (HSQC) nuclear magnetic resonance analysis. Reaction time: (a) 0 hour, (b) 6 hours, (c) 12 hours, (d) 18 hours, and (e) 24 hours. (f) Color coded structural motifs in lignin

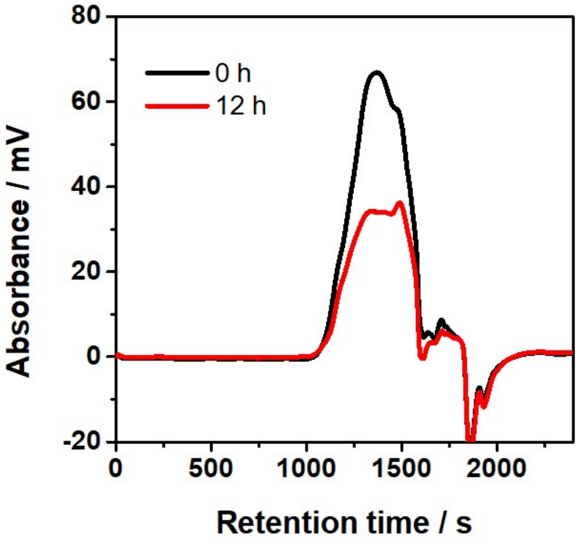

Figure S5. Gel permeation chromatography (GPC) analysis for the photoelectrochemical degradation of alkali lignin. The major fraction of untreated lignin was polymers of over 51,000 Mw and the photoelectrochemical reaction caused a significant decrease of the molecular weight to less than 15,000 Mw after prolonged reaction of 12 hours, which clearly showed fragmentation and degradation of lignin macromolecules. The newly appeared peak's height was not comparable to that of the initial peak, which implies that considerable amount of lignin was disintegrated into much smaller ones, not pertaining polymeric form.

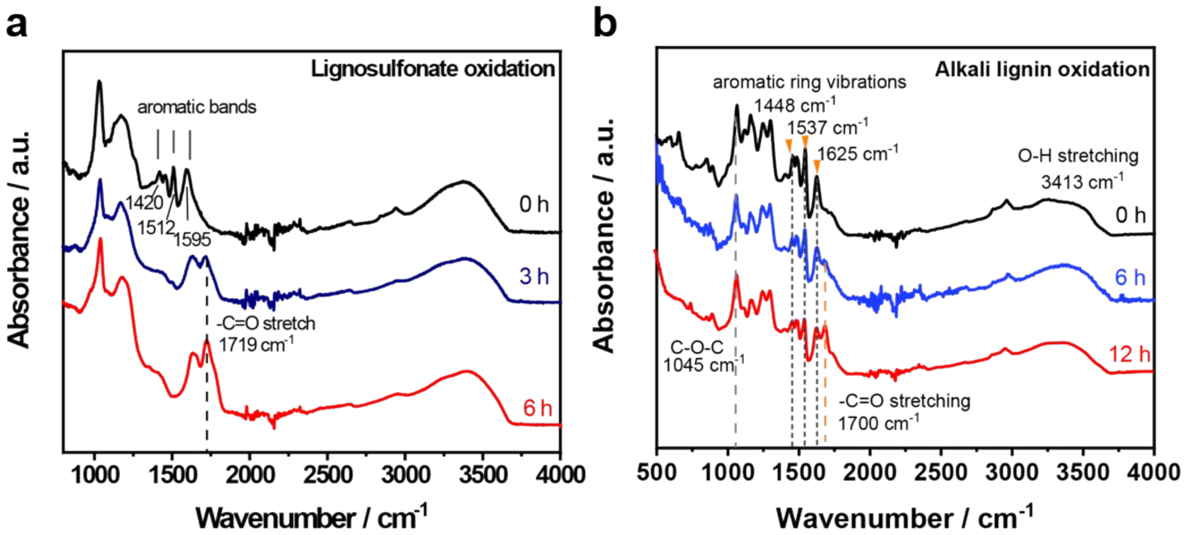

Figure S6. FTIR spectra of (a) lignosulfonate and (b) alkali lignin before and after oxidation. In single-cell component, $BiVO_4$ photoanode was immersed in a $KHCO_3$ buffer (10 mM, pH 8.2) containing 1 mg/ mL lignin under Xe lamp illumination (λ>400 nm) with 400 mV anodic bias, and a Pt wire was used as a counter electrode, $Ag/AgCl_{3M\ NaCl}$ was used as reference electrode.

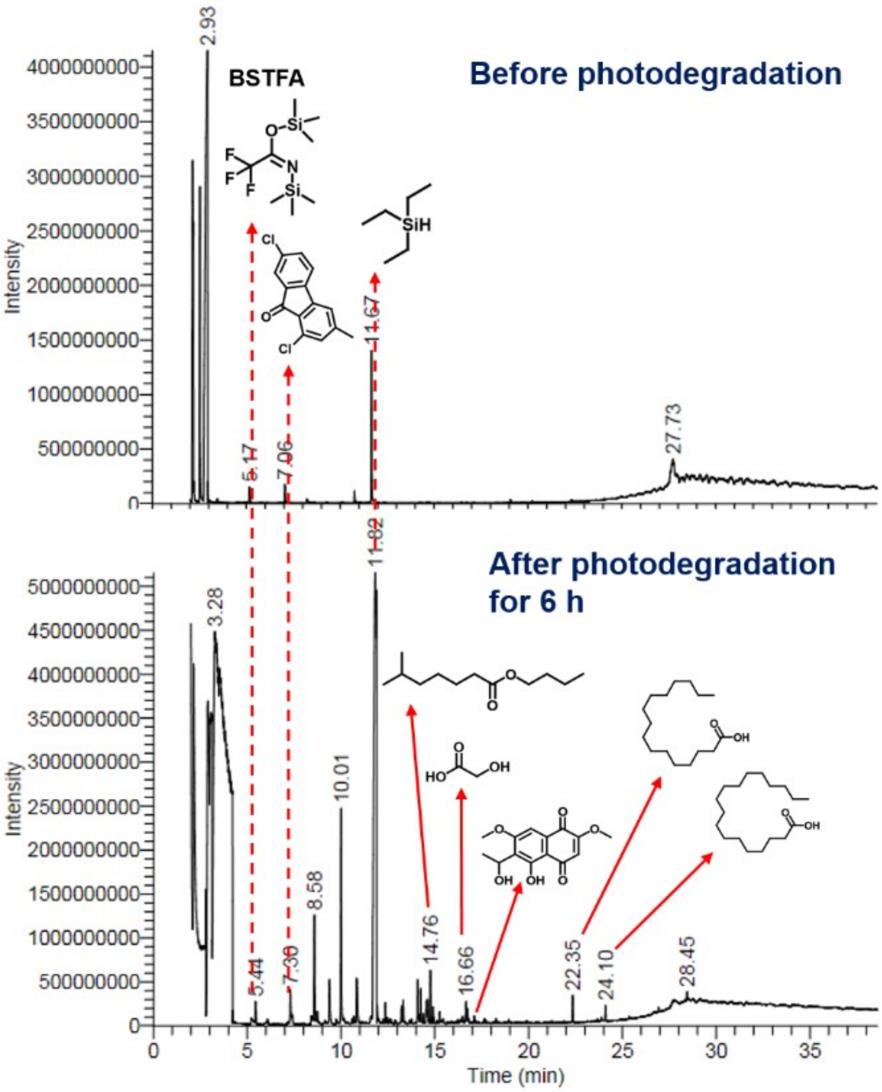

Figure S7. GC/MS analysis of lignosulfonate before and after degradation. Experimental conditions: in single-cell component, $BiVO_4$ photoanode was immersed in a $KHCO_3$ buffer (10 mM, pH 8.2) containing 1 mg/ mL lignosulfonate under Xe lamp illumination (λ>400 nm) with 400 mV anodic bias, and a Pt wire was used as a counter electrode, $Ag/AgCl_{3M\ NaCl}$ was used as reference electrode. Compounds were identified as TMS derivatives from oxidized lignosulfonate solution extracted with ethyl acetate.

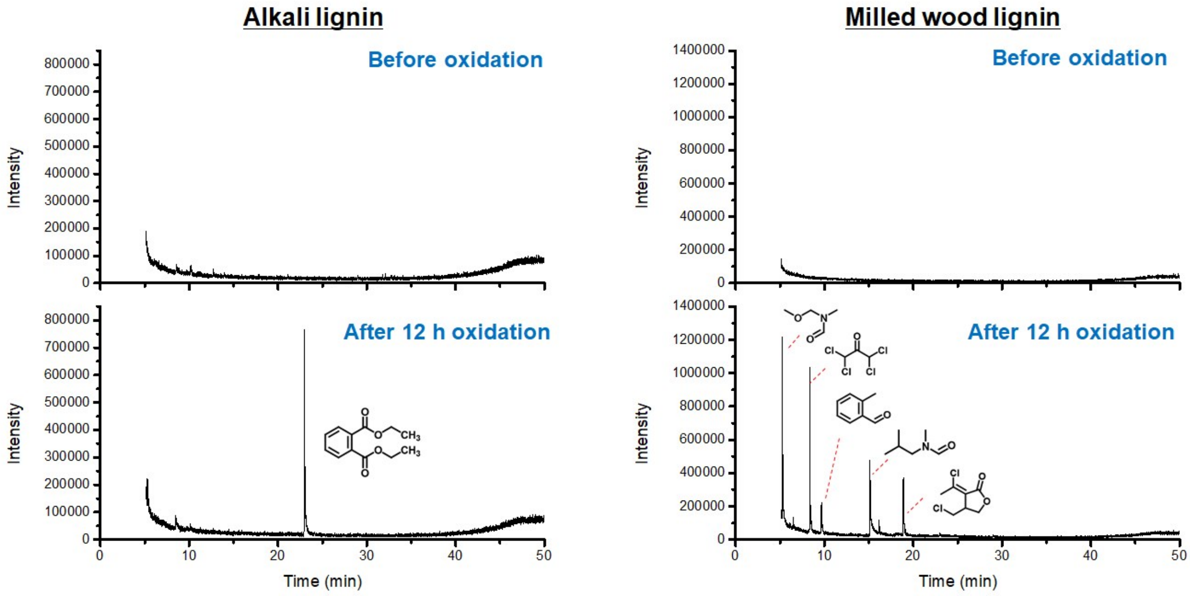

Figure S8. Gas chromatography/mass spectrometry (GC/MS) analysis of alkali lignin and milled wood lignin before and after oxidation. In a single-cell component, $BiVO_4$ photoanode was immersed in a $KHCO_3$ buffer solution (10 mM, pH 8.2) containing 1 mg mL^{-1} lignin under Xe lamp illumination (λ>400 nm) with 400 mV anodic bias. A Pt wire was used as a counter electrode and $Ag/AgCl_{3M\ NaCl}$ was used as a reference electrode.

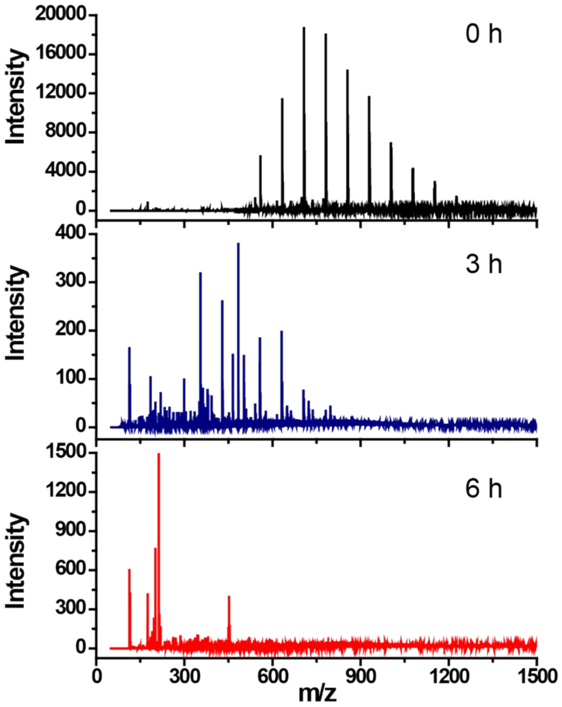

Figure S9. High resolution mass spectroscopy (HR-MS) analysis of lignosulfonate during degradation. The molecular weight distribution of lignosulfonate solution was decrease during the photoelectrochemical oxidation.

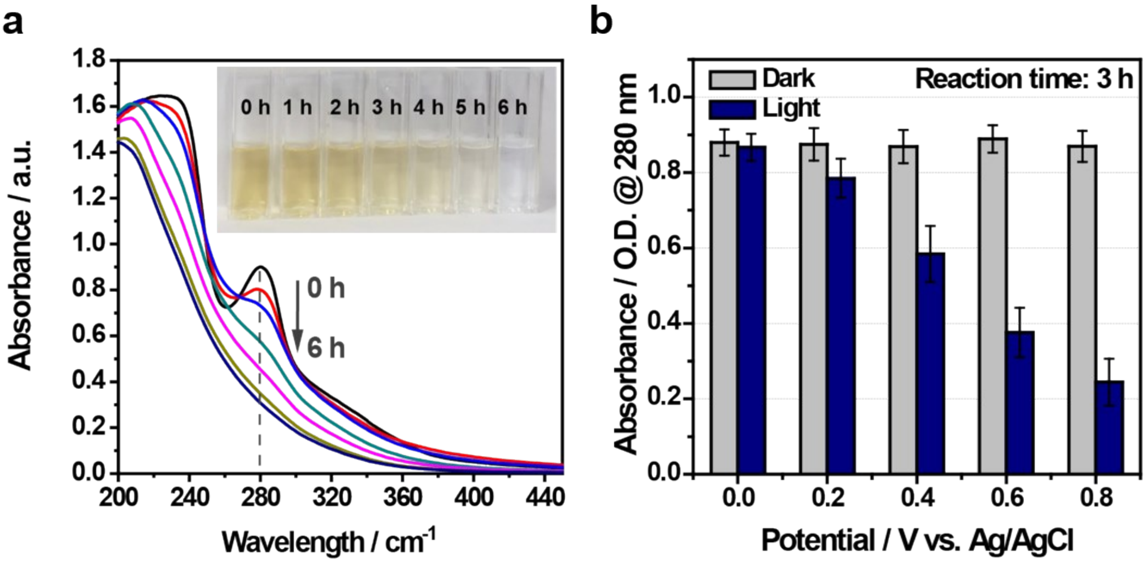

Figure S10. Photo-oxidation of lignosulfonate by $BiVO_4$ photoanode. (a) Change in UV-vis absorption spectrum of lignin solution (1 mg mL^{-1}) during its photodegradation by $BiVO_4$ with 0.4 V applied potential. (b) Change in absorbance of 1 mg mL^{-1} lignin solution at 280 nm with various applied potentials under dark or light conditions (100 mW cm^{-2}, reaction time: 3 h).

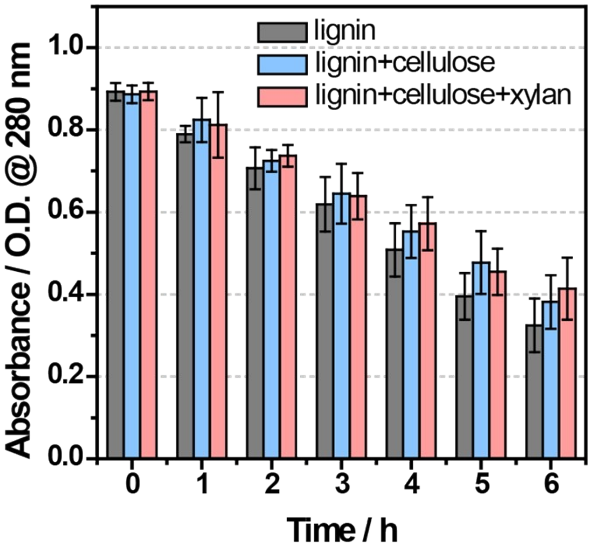

Figure S11. Photochemical degradation of lignin (1 mg mL^{-1}) using $BiVO_4$ electrode under the presence of cellulose and xylan (1 mg mL^{-1}) monitored by UV-vis absorption at 280 nm. Applied potential 0.4 V. The presence of additional components exhibited negligible effect on the oxidation of lignin by $BiVO_4$ even at the same concentration as lignin (1 mg mL^{-1}). The results suggest that $BiVO_4$ electrode oxidizes lignin (rather than other components) because of electrical activities of lignin originating from their diverse redox-active groups.

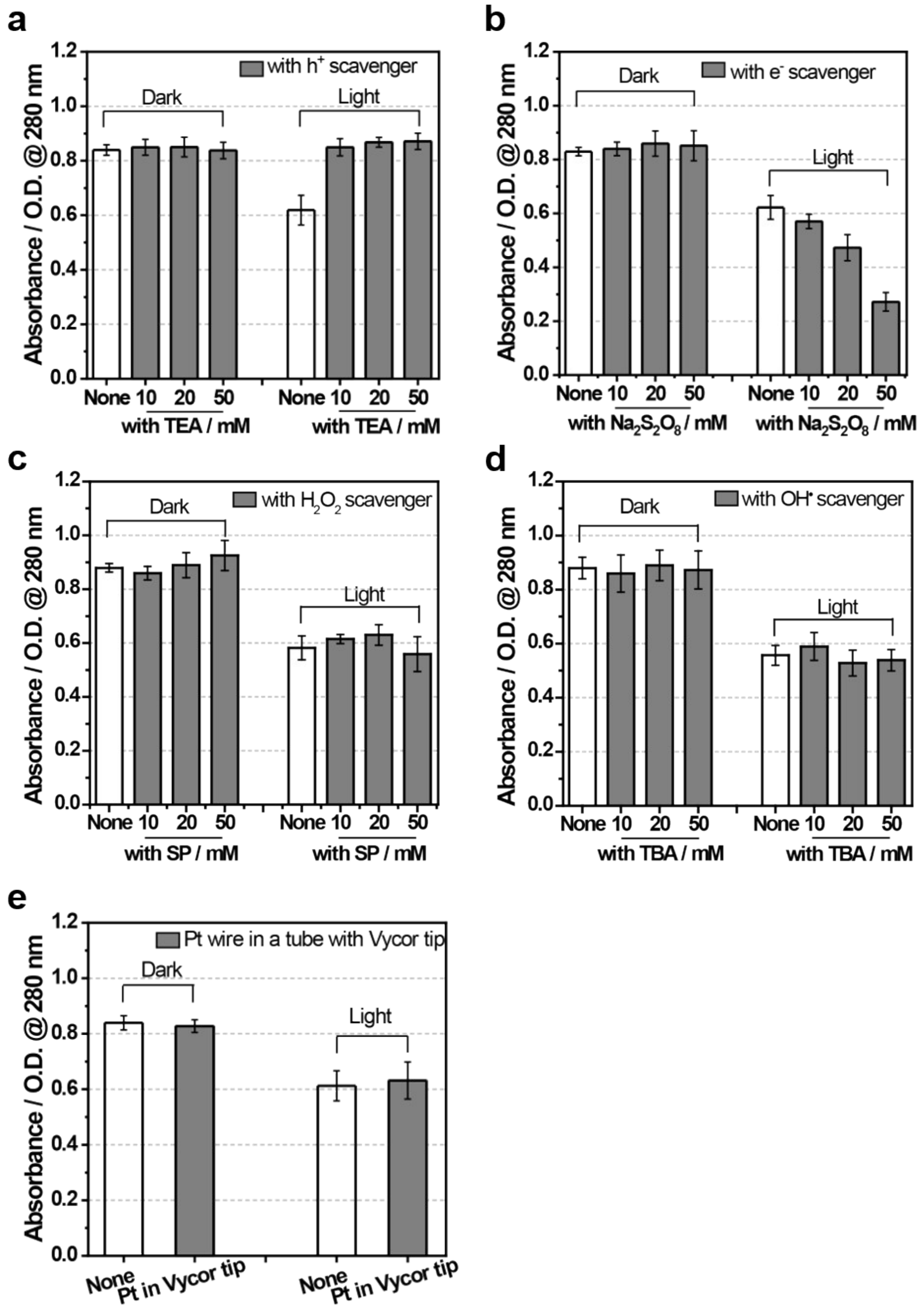

Figure S12. Effect of different kinds of scavengers on the oxidation of lignin by $BiVO_4$ photoanode under the applied potential of 400 mV (vs $Ag/AgCl_{3M\ NaCl}$) for 3 hours of light illumination (Xe lamp intensity: 100 mW cm^{-2}). Comparison of the absorption intensity at 280 nm of lignin photo-oxidized by $BiVO_4$ photoanode in the presence of scavengers (a) Triethylamine, TEA: hole scavenger, (b) sodium persulfate, $Na_2S_2O_8$: electron scavenger, (c) sodium pyruvate, SP: hydrogen peroxide scavenger, and (d) tert-butyl alcohol, TBA: hydroxyl radical scavenger. e) Effect of superoxide generation at the Pt counter electrode for the photoelectrochemical oxidation of lignin by $BiVO_4$ photoanode. The isolation of oxygen reduction reaction at the Pt counter electrode with a vycor tip membrane had negligible effect on the oxidation of lignin by $BiVO_4$.

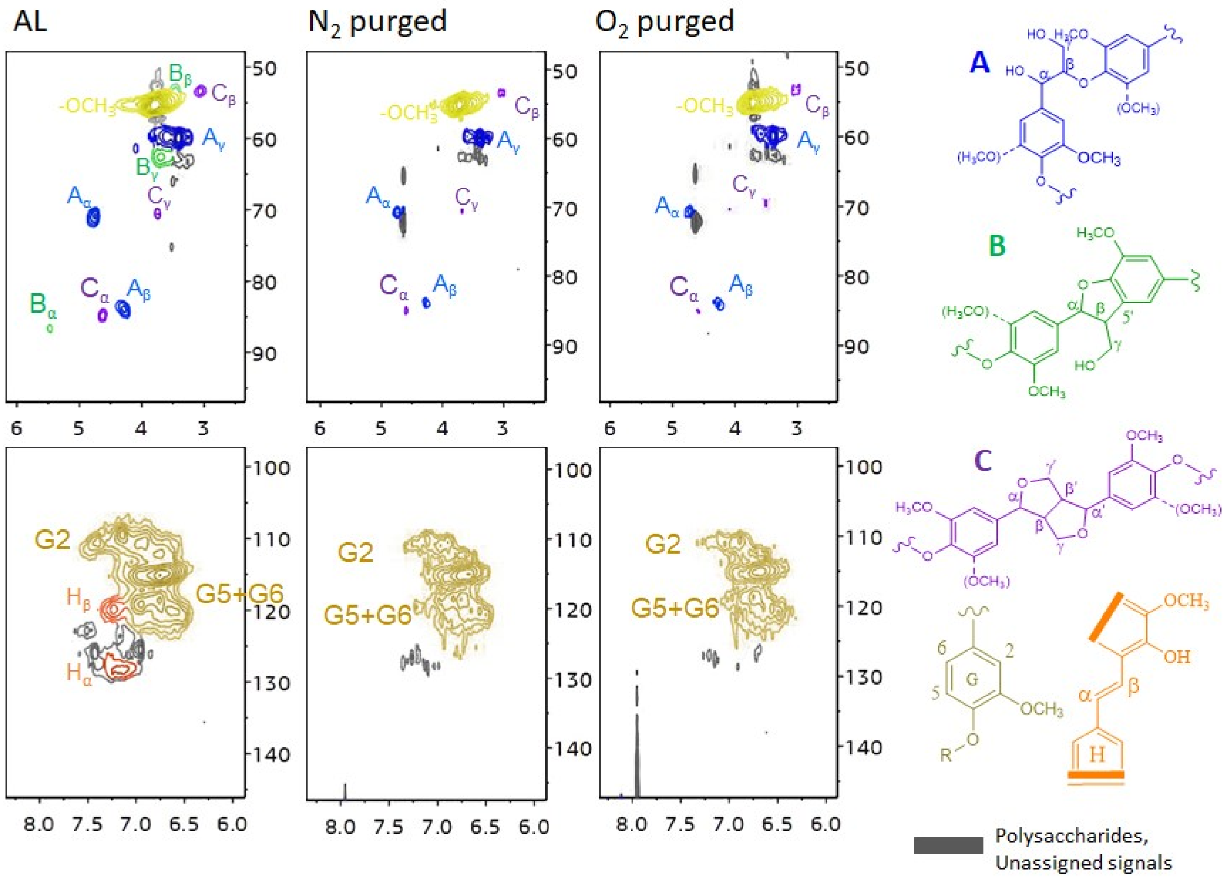

Figure S13. Changes in the chemical structure of alkali lignin (AL) of the photoelectrochemical oxidation process monitored by 2-dimentional ^{13}C-^{1}H heteronuclear single-quantum correlation (HSQC) nuclear magnetic resonance analysis. There was no significant difference in lignin oxidation after 12 hours under both of O_2 and N_2 purged conditions.

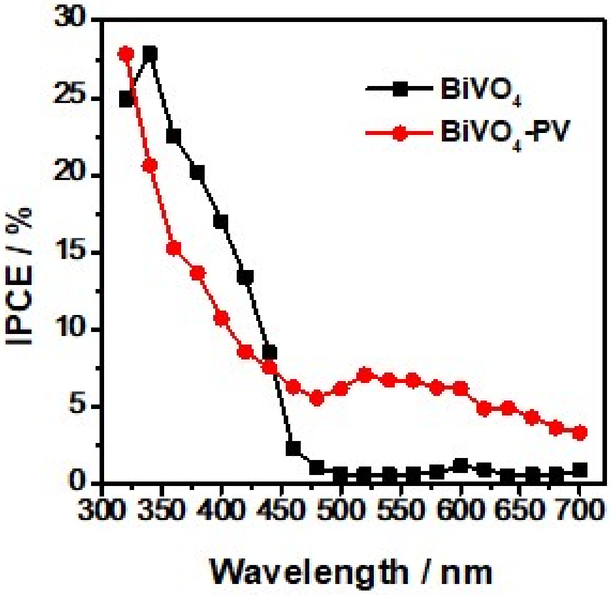

Figure S14. IPCE measurements of $BiVO_4$ and tandem $BiVO_4$-PV measured in a 10 mM bicarbonate buffer (pH 5) at 0 V versus $Ag/AgCl_{3M\ NaCl}$. While there was no photocurrent generation from bare $BiVO_4$ at above 450 nm, the $BiVO_4$-perovskite tandem system ($BiVO_4$-PV) maintained its photon-to-current efficiency up to 700 nm due to the photoexcitation by perovskite solar cell.

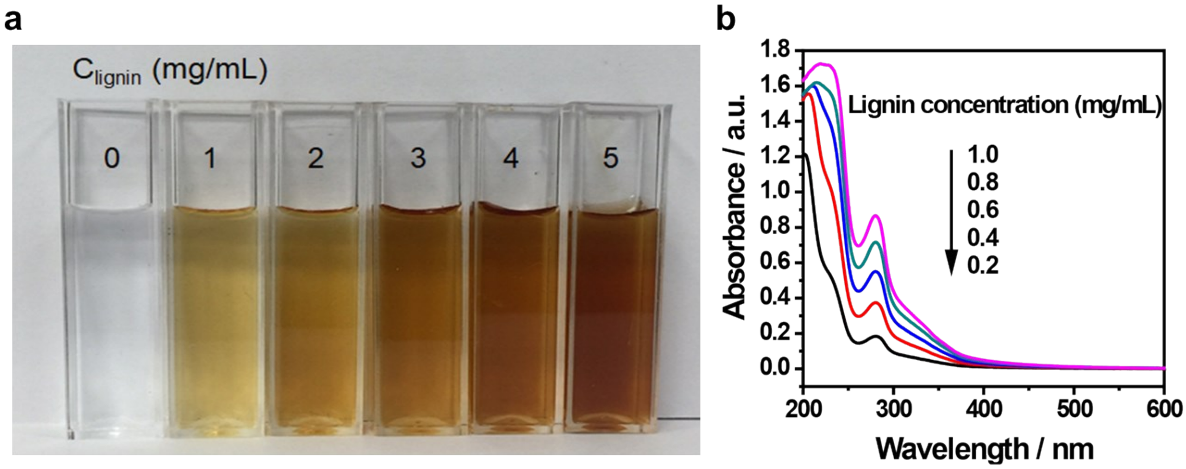

Figure S15. Optical property of lignosulfonate. (a) A photograph and (b) Spectral changes of lignin solutions with various lignosulfonate concentrations.

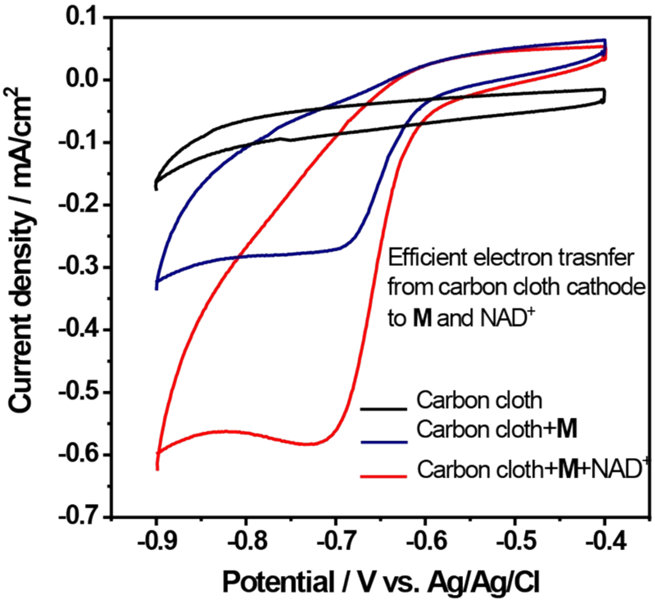

Figure S16. Electrochemical characterization of carbon cloth electrode for electrochemical NADH regeneration. The cyclic voltammograms of carbon cloth (black) revealed an increase of the cathodic current in the presence of **M** (blue) and NAD$^+$ (red). Experimental conditions: 0.5 mM **M**, 2 mM NAD$^+$ in a phosphate buffer (100 mM, pH 6.5). Scan rate: 50 mV s^{-1}.

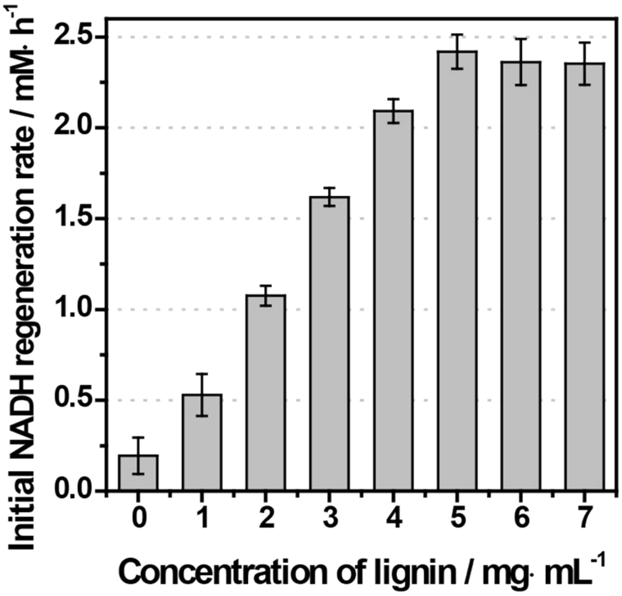

Figure S17. The rate of NADH regeneration with various lignin concentrations. Reaction conditions: Cathode electrolyte contained **M** (0.5 mM) and NAD$^+$ (2.0 mM) in a phosphate buffer (100 mM, pH 6.5).; Anode electrolyte contained 5 mg mL^{-1} lignin in a $KHCO_3$ buffer (10 mM, pH 8.2).; Geometrical surface area of $BiVO_4$, perovskite PV cell, and carbon cloth were 6, 1, and 2 cm^2, respectively.

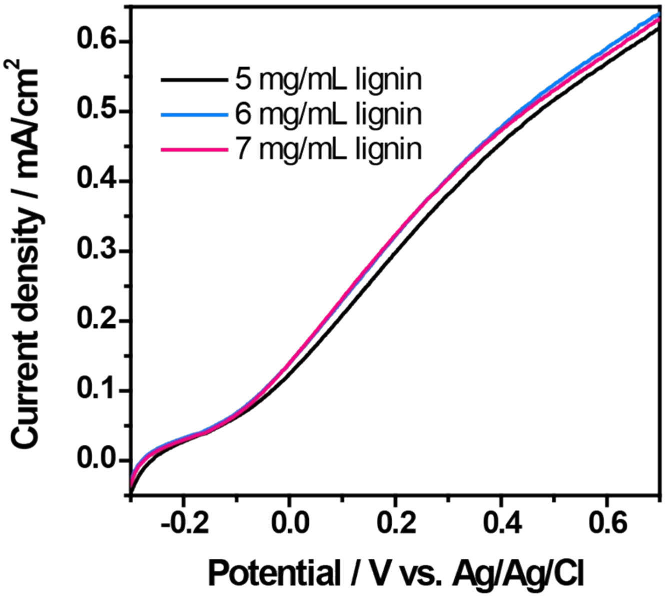

Figure S18. Linear sweep voltammogram (LSV) of the $BiVO_4$ photoelectrode with various concentrations of lignin under light irradiation. Experiment condition: Xe lamp intensity: 100 mW cm^{-2}, scan rate: 50 mV s^{-1}. At higher lignin concentrations, there was no enhancement in the photocurrent generation from $BiVO_4$.

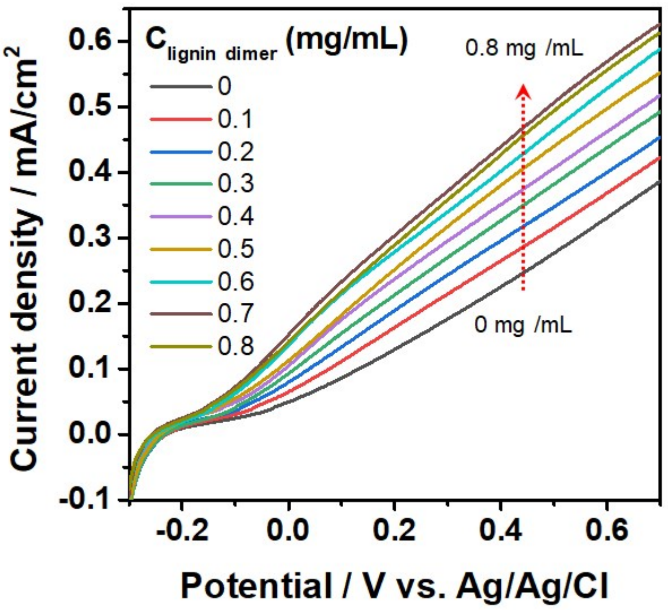

Figure S19. Linear-sweep voltammetric (LSV) of the $BiVO_4$ photoelectrode with various lignin model dimer (guaiacylglycerol-beta-guaiacyl ether) concentrations (0 ~ 0.8 mg mL^{-1}) under illumination (100 mW cm^{-2}). Scan rate: 50 mV s^{-1}.

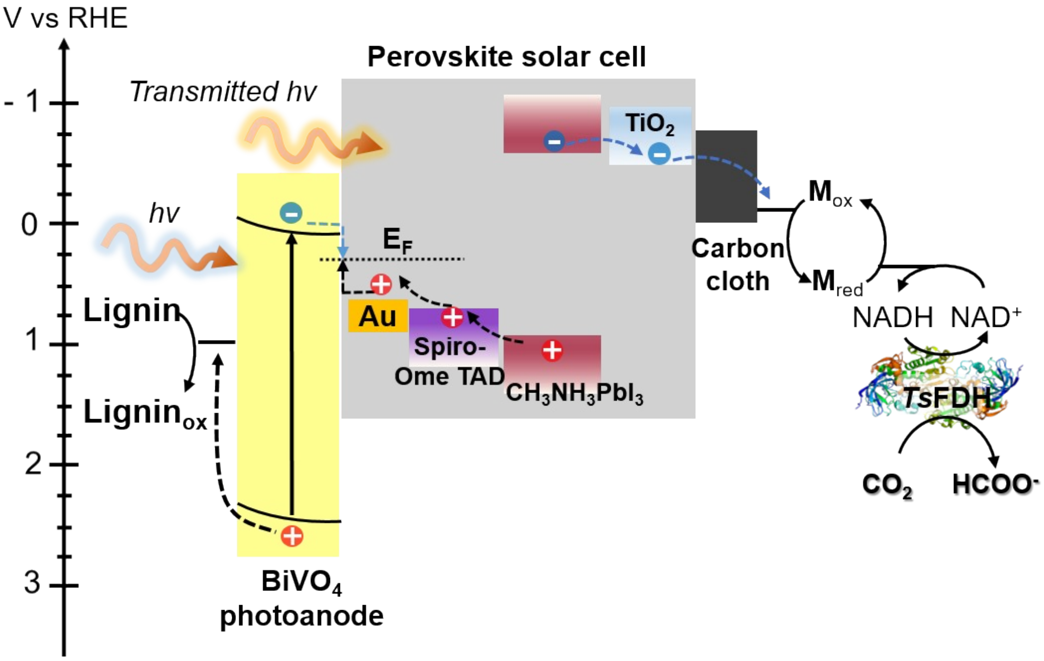

Figure S20. Schematic energy diagram of lignin-fueled PEC platform composed of $BiVO_4$/perovskite tandem photoanode and carbon cloth cathode for biocatalytic reduction of CO_2. CB: conduction band. VB: valence band.

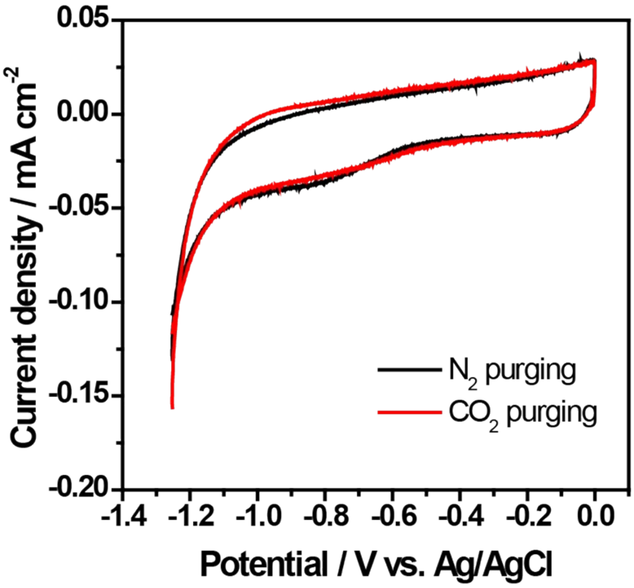

Figure S21. Cyclic voltammograms of carbon cloth electrode in the N_2 purged and CO_2 purged buffers. There was no sign of direct electrochemical reduction of CO_2.

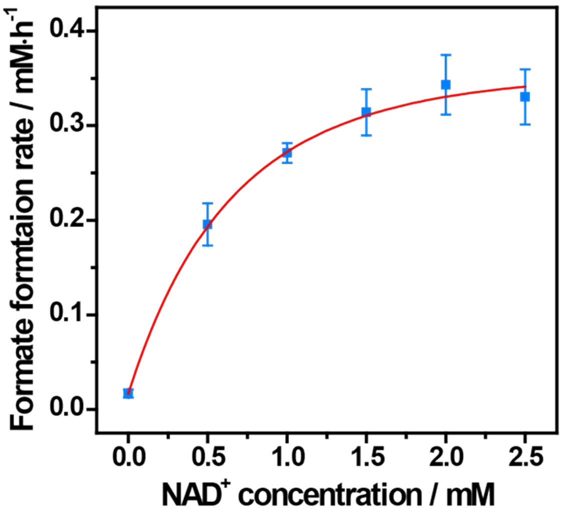

Figure S22. Influence of NAD$^+$ concentration on the enzymatic production of formate in the unbiased, lignin-fueled PEC system. Reaction condition: $BiVO_4$ was immersed in $KHCO_3$ buffer (10 mM, pH 8.2) containing 5 mg mL^{-1} lignin; in cathodic component, carbon cloth was immersed in a phosphate buffer (100 mM, pH 6.5) containing **M** (0.5 mM), *Ts*FDH (10 U mL^{-1}), and various concentration of NAD$^+$ with CO_2 bubbling. Geometrical surface area of $BiVO_4$, perovskite PV cell, and carbon cloth were 6, 1, and 2 cm^2, respectively.

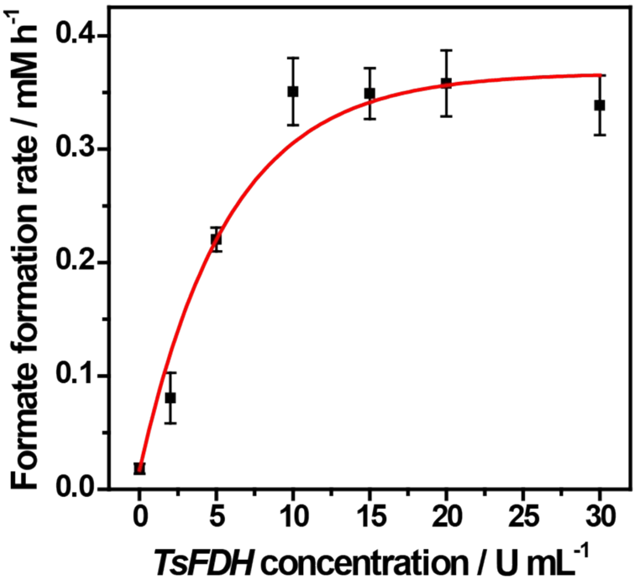

Figure S23. Photoelectrochemical formate production rate versus *Ts*FDH concentration. Reaction condition: $BiVO_4$ was immersed in $KHCO_3$ buffer (10 mM, pH 8.2) containing 5 mg mL^{-1} lignin; in cathodic component, carbon cloth was immersed in a phosphate buffer (100 mM, pH 6.5) containing **M** (0.5 mM), NAD$^+$ (2.0 mM), and various concentration of *Ts*FDH with CO_2 bubbling. Geometrical surface area of $BiVO_4$, perovskite PV cell, and carbon cloth were 6, 1, and 2 cm^2, respectively.

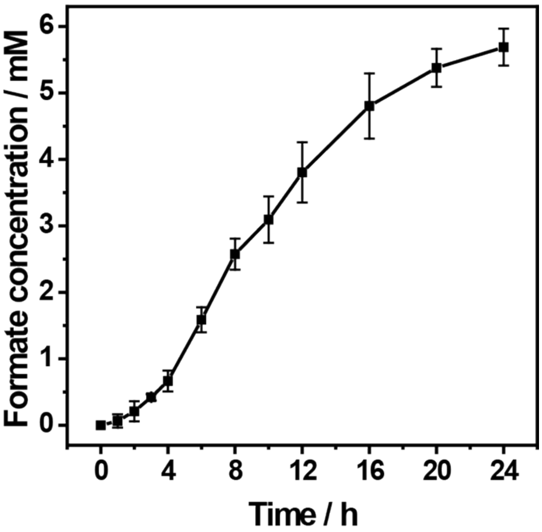

Figure S24. Time profiles of biocatalytic production of formate and photooxidation of lignin (1 mg mL^{-1}) in the photoelectrochemical platform.

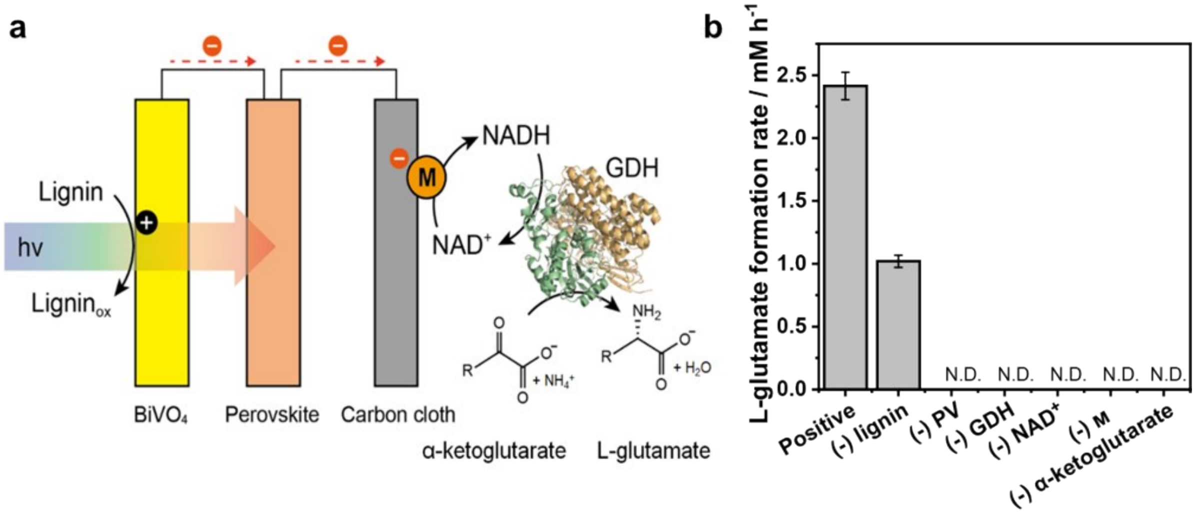

Figure S25. L-glutamate dehydrogenase (GDH) model reaction under lignin-fueled PEC system. (a) Schematic illustration for enzymatic conversion of α-ketoglutarate into L-glutamate under various reaction conditions. (b) A series of control experiments for the synthesis of L-glutamate in the unbiased tandem system

Table S1. Compounds identified from the oxidized alkali lignin solution.

Product	Structure	Retention time (min)
1-Methylpyrrolidin-2-one	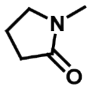	8.447
Diethyl phthalate	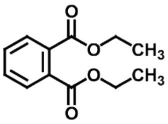	22.984

Table S2. Compounds identified from the oxidized milled wood lignin solution

Product	Structure	Retention time (min)
N-Methoxymethyl-N-methylformamide	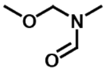	5.249
1,1,3,3-Tetrachloroacetone	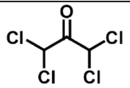	8.344
2-methylbenzaldehyde	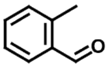	9.642
N-methyl-N(2-methylpropyl) formamide	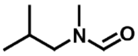	15.115
α-(1'-chloroethylidene)-β-(chloromethyl)-γ-butyrolactone	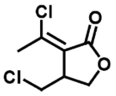	18.885

Table S3. Compounds identified as TMS derivatives from oxidized lignosulfonate solution extracted with ethyl acetate.

Product	Structure	Retention time (min)
Formic acid	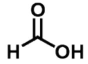	7.30
1,4-Dioxan-2-ol	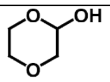	9.38
7,7-Dichloro-3,4-epoxy-4-isopropyl-1-methylbicyclo[4.1.0]-heptane	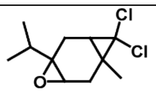	10.01
Acetic acid	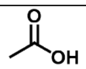	10.58
2-Ethoxyethanol	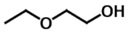	10.84
Benzoic Acid	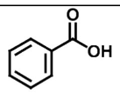	13.23
2-Butenedioic acid	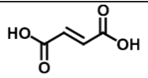	14.15
Butanedioic acid	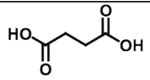	14.24
Butyl 6-methylheptanoate	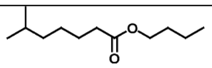	14.76
Erythrono-1,4-lactone	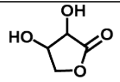	15.11
Pentanedioic acid	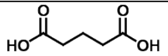	15.44
4H-1-Benzopyran-4-one,2-(3,4-dimethoxyphenyl)-3,5-dihydroxy-7-methoxy-	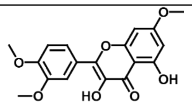	16.47
Glycolic acid	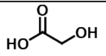	16.66
5-hydroxy-6-(1-hydroxyethyl)-2,7-dimethoxy-1,4-naphth oquinone	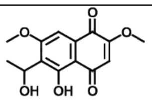	17.16
Palmitic Acid	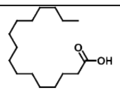	22.35
Stearic acid	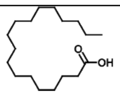	24.10

Table S4. Comparison of biocatalytic conversion of CO_2 to formate based on PEC platforms.

Photoelectrochemical platform		**Light range (nm)**	**Applied bias (V)**	**Major electron donor**	**Cofactor/FDH type**	**Operation time (h)**	**C_{avg}[a] (mM h^{-1})**	**Ref.**
(Photo)anode	**(Photo)cathode**							
Perovskite/$BiVO_4$	Carbon cloth	$\lambda > 400$	Unbiased	lignin	NADH/*Ts*FDH	24	0.246	This study
H-SiNW[b]	3-jn-Si/ITO/Co-Pi[c]	$\lambda > 420$	1.8	water	NADH/*Ts*FDH	6	0.0433	1
Co-Pi/α-Fe_2O_3	ITO	$\lambda > 420$	1.2	water	NADH/*Ts*FDH	5	0.11	2
Co-Pi/α-Fe_2O_3	$BiFeO_3$	$\lambda > 420$	0.8	water	NADH/*Cc*FDH[d]	6	0.338	3
IO-TiO2|dpp|POs-PSII[e]	IO-TiO_2	$\lambda > 420$	0.3	water	No cofactor / *DvH*FDH[f]	1	0.062	4

[a] Average rate of formate formation per reaction volume, [b] hydrogen-terminated silicon nanowires, [c] cobalt phosphate (Co-Pi) -deposited, npp+ triple-junction silicon on indium-tin oxide, [d] FDH from *Clostridium carboxidivorans* P7T, [e] PSII from *Thermosynechococcus elongatus*, dpp (a phosphonated diketopyrrolopyrrole dye), and POs [poly(1-vinylimidazole-co-allylamine)-[Os(bipy)2Cl]Cl redox polymer], [f] W- FDH from *Desulfovibrio vulgaris*.

Supplementary References

1. E. J. Son, J. W. Ko, S. K. Kuk, H. Choe, S. Lee, J. H. Kim, D. H. Nam, G. M. Ryu, Y. H. Kim and C. B. Park, *ChemComm.*, 2016, **52**, 9723-9726.
2. D. H. Nam, S. K. Kuk, H. Choe, S. Lee, J. W. Ko, E. J. Son, E.-G. Choi, Y. H. Kim and C. B. Park, *Green Chem.*, 2016, **18**, 5989-5993.
3. S. K. Kuk, R. K. Singh, D. H. Nam, R. Singh, J.-K. Lee and C. B. Park, *Angew. Chem. Int. Ed.*, 2017, **56**, 3827-3832.
4. K. P. Sokol, W. E. Robinson, A. R. Oliveira, J. Warnan, M. M. Nowaczyk, A. Ruff, I. A. C. Pereira and E. Reisner, *J. Am. Chem. Soc.*, 2018, **140**, 16418-16422.